Role of Electronic Passivation in Stabilizing the Lithium-$Li_xPO_yN_z$ Solid-Electrolyte Interphase

Yuheng Li,[1] Pieremanuele Canepa,[1,2,*] and Prashun Gorai[3,†]

[1] *Department of Materials Science and Engineering, National University of Singapore, 9 Engineering Drive 1, 117575, Singapore*

[2] *Department of Chemical and Biomolecular Engineering, National University of Singapore, 4 Engineering Drive 4, 117585, Singapore*

[3] *Colorado School of Mines, Golden, Colorado 80401, USA*

(Received 22 March 2022; revised 27 June 2022; accepted 29 June 2022; published 4 August 2022)

The solid-electrolyte interphase (SEI) is crucial to the electrochemical performance of all-solid-state batteries (ASSBs). Theoretical characterization of SEI properties will help understand the origin of interfacial stability (and instability) between solid electrolytes and electrodes. Among solid electrolytes for Lithium (Li)-ion ASSBs, the lithium phosphorus oxynitride $Li_xPO_yN_z$ (LiPON) is one of the most stable against the Li metal anode. However, it has been shown that LiPON reacts with Li metal and forms SEIs. The SEI formation stops after a thin layer is formed, but the mechanism that enables this apparent stabilization is unclear. Thermodynamics underpins the defect formation in materials and, in turn, creation of electronic charge. Materials for energy storage, including solid electrolytes, are no exception to this fundamental process. Here, we computationally evaluate the electronic passivation of SEIs and its role in stabilizing the Li-LiPON interface. Specifically, we determine the defect and charge carrier concentrations in Li-LiPON SEIs, including Li_2O, Li_3N, Li_3P, and Li_3PO_4. The defect and charge carrier concentrations are calculated from defect thermodynamics. We then predict the electronic conductivities of the SEIs under different electrochemical conditions, which correspond to varying potentials to the Li metal anode. Our results reveal that the stoichiometrically abundant and uniformly distributed Li_2O has expectedly negligible electronic conductivity, while the electronically conducting components, such as Li_3N and Li_3P, show preferential distribution in the SEI. We posit that the overall electronically insulating nature of the SEI is responsible for the stability of the Li-LiPON interface. The computational approach adopted here can be extended to reveal the origin of the interfacial stability in other ASSBs.

DOI: 10.1103/PRXEnergy.1.023004

I. INTRODUCTION

In the context of global decarbonization, rechargeable alkali-ion batteries have become one of the key enabling technologies for sustainable energy storage [1–3]. All-solid-state batteries (ASSBs) that incorporate inorganic solid electrolytes in place of flammable liquid electrolytes have drawn considerable attention due to their potentially improved safety, and high power density [4–8]. However, there are significant challenges in developing solid electrolytes for ASSBs, especially those related to the interfacial instability with alkali-metal anodes [8–10].

The interfacial stability in ASSBs, which largely depends on the formation and chemical and electronic properties of solid-electrolyte interphases (SEIs), has been a central topic in battery research [11–13]. Interfaces formed between solid electrolytes and electrodes can be classified into three types according to the formation and properties of the SEIs [13]: (1) stable interfaces with no decomposition SEIs, (2) interfaces formed with SEIs that conduct both electrons and alkali ions, and (3) interfaces formed with stable SEIs that are electronically insulating. Electronically insulating SEIs ensure that the interface is electronically passivated, i.e., it prevents progressive chemical decomposition of the electrode and electrolyte. Despite their importance, detailed characterizations of the composition, morphology, and spatial distribution of SEIs is still limited due to metrological challenges. The characterization of the electronic transport in SEIs is even

*pcanepa@nus.edu.sg
†pgorai@mines.edu

more challenging, and is inferred only indirectly from device-level electrochemical measurements.

The glassy lithium phosphorus oxynitride $Li_xPO_yN_z$ (with unknown stoichiometry), termed LiPON, is one of the few lithium (Li)-ion solid electrolytes considered to be electrochemically "stable" against a Li-metal anode [14–20]. The chemical composition of LiPON, let aside its structure, has been the subject of many studies [15,19,20]. A cycle life of 10 000 with 90% capacity retention has been claimed for ASSBs incorporating LiPON electrolyte paired with a high-energy density Li-metal anode and a spinel $LiNi_{0.5}Mn_{1.5}O_4$ cathode [21]. Despite the good interfacial stability indicated by the device performance, first-principles calculations have shown that the decomposition of LiPON and the consequent formation of Li-LiPON SEIs are thermodynamically favorable [9,11,13]. LiPON reacts with Li and decomposes to binary Li_2O, Li_3N, and Li_3P and ternary Li_3PO_4 [12,13,22]. The fact that LiPON reacts with Li metal seems contradictory to the interfacial stability, but the reaction shows self-passivating behavior, which stabilizes the interface. It is believed that progressive LiPON decomposition is prevented after a "thin" SEI layer forms and serves as a passivating layer that limits electron transfer, while still allowing facile Li-ion transport.

Recently, the formation and structure of Li-LiPON SEIs have been investigated with different microscopy and spectroscopic techniques (Fig. 1). *In situ* x-ray photoemission spectroscopy (XPS) probed surface species on LiPON exposed to Li vapor [22]. The XPS spectra indicated that Li_2O, Li_3N, Li_3P, and Li_3PO_4 form after a short exposure, but then the signals for Li_3N and Li_3P become less intense after a longer exposure time. More recent experiments with cryogenic transmission electron microscopy (TEM) and XPS depth profiling revealed the presence of Li_2O, Li_3N, and Li_3PO_4, as well as a thin multilayer-mosaic structure with N and P concentration gradients (high concentrations near the LiPON side and absent near the Li side) for the Li-LiPON SEI [23]. *In situ* TEM observed the evolution of LiPON contacting Li under bias [24]. An approximate 60-nm-thin layer forms at the Li-LiPON interface, where P species show preferential spatial distribution and do not appear in direct contact with Li metal. While these studies have been insightful in understanding the chemical makeup and spatial distribution of the SEI, the fundamental mechanism that lends to the self-passivating behavior is still unclear. Complementary theoretical modeling can provide further insights into the electronic origin of the self-passivation.

One hypothesis for the self-passivation mechanism is that electron transfer is suppressed after the initial SEI formation so that LiPON decomposition is prevented. To confirm this hypothesis, we need to characterize the electronic conductivity of the SEI components. Notably, band-gap energy, though often used, is not a reliable descriptor of

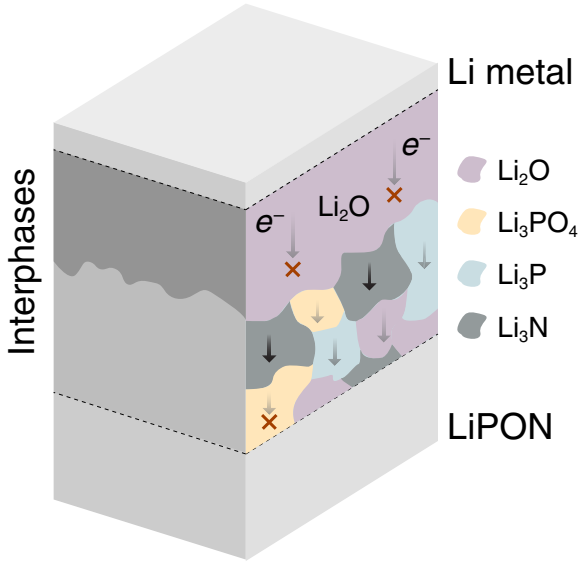

FIG. 1. Schematic of the Li-LiPON SEIs. Previous experimental studies have shown that Li_2O, Li_3N, Li_3P, and Li_3PO_4 are the primary decomposition products present in the Li-LiPON SEI. The spatial distribution of the SEIs' components shown in this schematic are only for representative purposes, and inspired by existing detailed experimental characterizations [22–24].

electronic conductivity. Indeed, it is impossible to establish any empirical relationship between the band gap and electronic conductivity for solid electrolytes [25]. Instead, one should assess charged defects as the major source of free charge carriers and the resulting electronic conductivity. Based on defect calculations, our previous study has successfully predicted the electronic conductivity in different types of solid electrolytes including Li_6PS_5Cl and Li_6PS_5I argyrodites and Na_3PS_4 [25].

In this study, we use first-principles defect calculations to predict the electronic conductivity in the Li-LiPON SEI components, Li_2O, Li_3N, Li_3P, and Li_3PO_4. We estimate the net free charge carrier concentrations from defect thermodynamics, which are then used with estimated carrier mobilities to determine the electronic conductivity under different (electro)chemical limits or voltages versus Li/Li^+. In combination with the previous experimental observations of the elemental distributions, we reveal that the SEI electronic self-passivation originates from the insulating nature of the stoichiometrically dominant Li_2O and uneven distribution of the electronically conductive species Li_3N and Li_3P.

II. RESULTS

We first discuss the phase equilibria of the SEI components to obtain their accessible range of electrochemical conditions or voltages versus Li/Li^+. Then, we present the native defect chemistry of the SEI components under the identified electrochemical conditions, including the defect

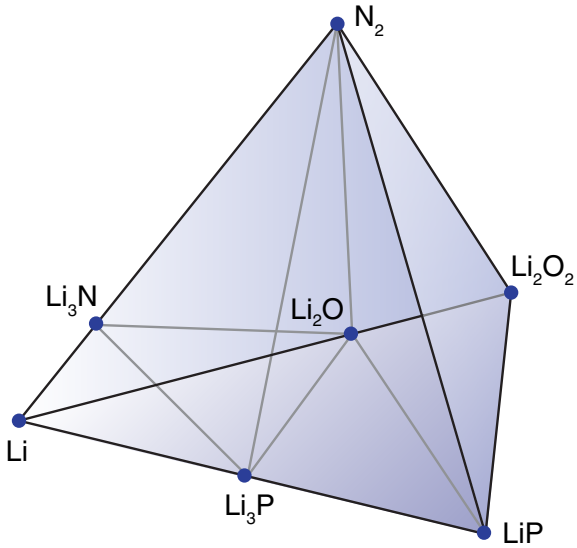

FIG. 2. Phase diagram showing the phase equilibria of the binary Li-LiPON interphase components: Li_2O, Li_3N, and Li_3P. Phases in equilibrium in the Li-LiP-Li_2O_2-N_2 chemical space are connected by tie lines.

formation energy, the equilibrium Fermi energy, the defect concentration, and the net free charge carrier concentration. We predict the electronic conductivity of the SEI components based on the predicted carrier concentrations and estimated carrier mobilities.

A. Phase equilibria of Li-LiPON interphases

The formation energy of defects depends on the chemical potentials of the elements associated with a defect [Eq. (2) below]. For a given compound, the accessible range of chemical potentials is set by the phase stability in the compound phase diagram obtained through a convex hull analysis [26]. We investigate the thermodynamically stable phases in the quaternary Li-P-O-N chemical space. Figure 2 shows the quaternary phase diagram containing the SEI binaries. We use Li, LiP, Li_2O_2, and N_2 as the end members. Elemental oxygen and phosphorous are not used because they are less relevant in either the synthesis of LiPON or the interfacial reactions [14,15,22]. Notably, the ternary SEI component Li_3PO_4 lies outside of this phase diagram. Because of its complex phase equilibria, the phase diagram of Li_3PO_4 is discussed separately in Sec. II E.

In Fig. 2, we show the thermodynamically stable phases that lie on the convex hull. Compositions not marked by dots represent situations of phase separation into the stable compounds encompassing them. In addition, every tie line shows that its two end members are in thermodynamic equilibrium.

As an example, Li_3P is in equilibrium with elemental Li and LiP. It is evident that Li metal represents the most Li-rich limit (most reducing condition) and LiP the most Li-poor (most oxidizing) limit for Li chemical potential (μ_{Li}). A more Li-rich chemical condition corresponds to a more reducing electrochemical situation in batteries, or a lower voltage versus Li/Li^+. One can also find that there is only one independent variable of elemental chemical potential in the binary Li_3P. Mathematically, $3\Delta\mu_{Li} + \Delta\mu_P = \Delta G_f(Li_3P) \approx \Delta H_f(Li_3P)$, where $\Delta G_f(Li_3P)$ is the free energy of formation, approximated by the formation enthalpy $\Delta H_f(Li_3P)$ of Li_3P (a constant). Here, $\Delta\mu_{Li} = \mu_{Li} - \mu^0_{Li}$, with $\Delta\mu^0_{Li}$ being the elemental Li reference chemical potential. The range of $\Delta\mu_{Li}$ that ensures phase stability of Li_3P is then calculated by imposing the condition of instability of LiP, i.e., $\Delta\mu_{Li} + \Delta\mu_P < \Delta H_f(LiP)$, and the condition of instability of elemental Li, i.e., $\Delta\mu_{Li} < 0$. Likewise, the accessible range of $\Delta\mu_{Li}$ for Li_2O is constrained by Li and Li_2O_2, and Li_3N by Li and N_2. The accuracy of the calculated formation enthalpies of the SEI components, which are used to obtain the accessible ranges of elemental chemical potentials, are discussed in Sec. S1 of the Supplemental Material [27]. The effect of the uncertainty in calculated formation enthalpies on the estimated electronic conductivity is also discussed in Sec. S1. The calculated $\Delta\mu_{Li}$ limits for each binary component are converted to voltages versus Li/Li^+ and listed at the top of Figs. 3–5 below. The $\Delta\mu$ of relevant elements in each SEI component under different chemical conditions are listed in Tables S3–S6 within the Supplemental Material [27].

B. Native defect chemistry of Li_2O

Li_2O is a highly stable oxide and a common SEI component at the Li anode when the electrolyte contains oxygen [13]. We calculate the formation energy of native defects in Li_2O as a function of the Fermi energy (Fig. 3). The Fermi energy (E_{Fermi}) is referenced to the valence-band maximum (VBM), i.e., $E_{Fermi} = 0.0$ eV at VBM. The highly ionic Li_2O has an ultrawide band gap of about 8.01 eV (with the *GW* approximation), which sets the conduction-band minimum to $E_{Fermi} = 8.01$ eV. It is notable that the *GW* approximation tends to slightly overestimate experimental band gaps of ultrawide band-gap battery materials [25]. We consider the two limiting thermodynamic conditions within the region of phase stability: (i) most Li-rich condition (reducing) corresponding to equilibrium with metallic Li ($\Delta\mu_{Li} = 0$ eV, voltage versus Li/Li^+ is 0 V) and (ii) most Li-poor condition (oxidizing) corresponding to equilibrium with Li_2O_2 ($\Delta\mu_{Li} = -3.02$ eV, voltage versus Li/Li^+ is 3.02 V). Figures 3(a) and 3(b) show the defect formation energies under the most Li-rich and most Li-poor conditions, respectively. In Fig. 3 and subsequent defect plots, all unique Wyckoff sites for each defect type are considered and plotted. In Li_2O, there is only one unique Wyckoff site each for Li and O.

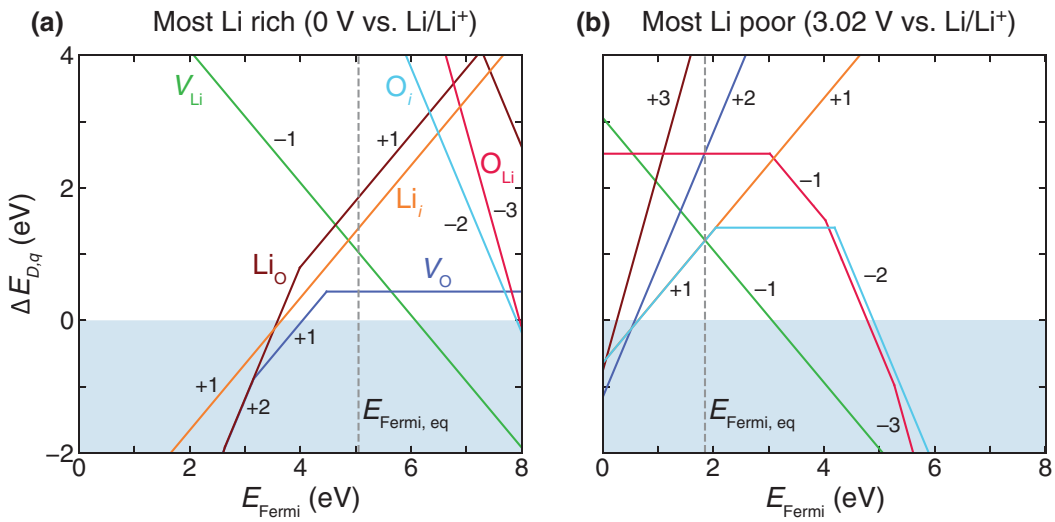

FIG. 3. Formation energy ($\Delta E_{D,q}$) of native point defects in Li_2O as a function of Fermi energy (E_{Fermi}) under (a) the most Li-rich or reducing ($\Delta\mu_{\text{Li}} = 0$ eV, voltage versus Li/Li^+ is 0 V) and (b) the most Li-poor or oxidizing ($\Delta\mu_{\text{Li}} = -3.02$ eV, voltage versus Li/Li^+ is 3.02 V) conditions within the phase stability region constrained by Li and Li_2O_2. In this and all the following defect plots, Fermi energy is referenced to the valence-band maximum. Formation energies for different defect types are plotted in different colors. Multiple lines of the same color represent defects at multiple unique Wyckoff sites. Only the lowest-energy charge state is plotted for each defect. The vertical dashed line marks the equilibrium Fermi energy calculated at 300 K.

The slopes of the defect lines are the charge states of the defects, as evident from Eq. (2) below. A broad set of plausible charge states are calculated for each defect type, but conventionally only the most favorable charge states are shown. The vertical dashed lines denote the equilibrium Fermi energy ($E_{\text{Fermi,eq}}$), which is obtained through a self-consistent search to fulfill charge neutrality of charged defects and electronic charge carriers in the material [25, 28]. In the self-consistent search, the defect concentration is calculated from the defect formation energy through a Boltzmann distribution, i.e., $[X^q] = N_s e^{-\Delta E_{D,q}/k_B T}$, where $[X^q]$ is the defect concentration, N_s is the concentration of the lattice sites where the defect can be formed, $\Delta E_{D,q}$ is the defect formation energy, k_B is the Boltzmann constant, and T is the temperature. The blue shaded region is where the defect formation energies are negative, i.e., defects form spontaneously. As shown in the following results, $E_{\text{Fermi,eq}}$ is always located where all defects have positive formation energies.

Typically, it is assumed that defects formed at high formation temperatures ($T_{\text{formation}}$) are "frozen in" due to the large kinetic barriers at lower temperatures that prevent their reequilibration. However, the SEI between Li and LiPON forms spontaneously at temperatures lower than 100 °C [7,8]. As such, we expect defect formation in the SEI components at these lower temperatures. Therefore, for all the SEI components in this study, we consider that the defects are "frozen in" in the $T_{\text{formation}}$ range of 300–500 K, which is from room temperature to higher temperatures that might be reached due to the exothermic nature of the LiPON decomposition reactions [13].

Under the most Li-rich or reducing condition [Fig. 3(a)], $E_{\text{Fermi,eq}}$ is at 5.05 eV (300 K) and 5.04 eV (500 K). Note that the decrease of $E_{\text{Fermi, eq}}$ from 300 to 500 K is within 6 meV, which is indiscernible in the figure, so the vertical dashed line is representative of $E_{\text{Fermi, eq}}$ throughout the temperature range of interest. At $E_{\text{Fermi,eq}}$, the dominant defects are V_O^0, V_{Li}^{-1}, Li_i^{+1}, and Li_O^{+1}, and the defect formation energies of the charged defects are all above 1 eV. Defect V_O is a deep defect characterized by charge transition levels inside the band gap. The existence of midgap states are confirmed in the calculated density of states for V_O in Li_2O (see Fig. S1 within the Supplemental Material [27]). When the temperature is raised to 500 K, $\Delta E_{D,q}$ for a $q = +1$ ($q = -1$) defect decreases (increases) by 6 meV, in line with the change in $E_{\text{Fermi,eq}}$. The defects that mediate Li diffusion have total concentrations of the orders of 10^5 cm^{-3} (300 K) and 10^{12} cm^{-3} (500 K). At 300–500 K, the net free electron concentration (n) is negligible under the most Li-rich condition (equilibrium with Li metal) The difference in the defect thermodynamics is negligible between the $T_{\text{formation}}$ of 300 and 500 K. Such negligible differences do not alter our conclusions, qualitatively or quantitatively, and therefore in the rest of Sec. II we focus only on the results calculated for $T_{\text{formation}}$ of 300 K. Complete results for the defect thermodynamics for $T_{\text{formation}}$ of both 300 and 500 K can be found in Tables S3–S6 within the Supplemental Material [27].

Under the most Li-poor or oxidizing conditions [Fig. 3(b)], $E_{\text{Fermi,eq}}$ is at 1.85 eV. The dominant defects are V_{Li}^{-1}, Li_i^{+1}, and O_i^{+1}, and their $\Delta E_{D,q}$ are very close to each other (1.21 eV) at the $E_{\text{Fermi,eq}}$. Note that the oxygen

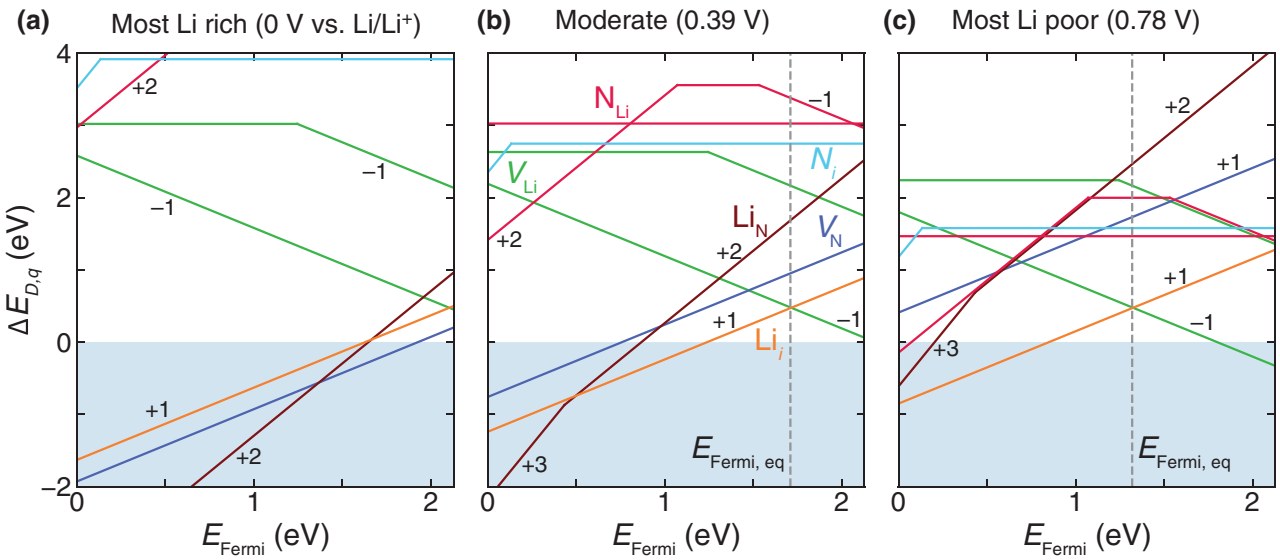

FIG. 4. Formation energy of native point defects in Li_3N as a function of the Fermi energy under (a) the most Li-rich ($\Delta\mu_{Li} = 0$ eV, voltage versus Li/Li^+ is 0 V), (b) moderate, and (c) the most Li-poor ($\Delta\mu_{Li} = -0.78$ eV, voltage versus Li/Li^+ is 0.78 V) conditions within the phase stability region constrained by Li and N_2. Multiple lines of the same color represent defects at multiple unique Wyckoff sites.

interstitial O_i exhibits amphoteric behavior, i.e., it is positively charged at Fermi energies closer to the valence band and negatively charged at Fermi energies closer to the conduction band. The Li-related dominant defects have a total concentration of 6.1×10^2 cm^{-3}. The defects with positive and negative charges show almost identical concentrations, and the net free carrier concentration is negligible. Note that the carrier (hole) concentration can reach 10^9 cm^{-3} at a synthesis temperature of 800 K though such high temperatures are not accessible during the formation of the Li-LiPON SEI.

It is clear that Li_2O has negligible net free charge carriers in the accessible range of thermodynamic equilibrium conditions and relevant formation temperatures. As such, Li_2O is a highly insulating SEI component.

C. Native defect chemistry of Li_3N

One of the Li-LiPON decomposition products is Li_3N, which has previously been investigated extensively as a Li-ion conductor [29–32]. However, its electronic conductivity has not been discussed extensively. Figure 4 shows the defect formation energy for Li_3N as a function of the Fermi energy (E_{Fermi}). We calculate the band gap of Li_3N to be about 2.13 eV from the *GW* approximation, which sets the *x*-axis range in Fig. 4. We examine the defect energetics under three representative thermodynamic conditions [Figs. 4(a)–4(c)] in the accessible range: the most Li rich or reducing ($\Delta\mu_{Li} = 0$ eV), moderate ($\Delta\mu_{Li} = -0.39$ eV), and the most Li poor or oxidizing ($\Delta\mu_{Li} = -0.78$ eV).

Under the most Li-rich condition [Fig. 4(a)], $E_{Fermi,eq}$ is at 2.17 eV, which is inside the conduction band (not shown). This indicates that Li_3N is degenerately *n* type under Li-rich conditions. In other words, Li_3N has high free electron concentration. The calculated net free electron concentration is of the order of 10^{18} cm^{-3}. The dominant defects at $E_{Fermi,eq}$ are V_N^{+1}, V_{Li}^{-1}, and Li_i^{+1}. The total concentration of V_{Li}^{-1} and Li_i^{+1}, which mediate Li diffusion, is over 10^{15} cm^{-3}. This agrees well with experimental findings that Li_3N is a good Li-ion conductor [32].

Under the most Li-poor condition [Fig. 4(c)], $E_{Fermi,eq}$ is at 1.32 eV. The dominant defect is Li_i^{+1}, with a very low $\Delta E_{D,q}$ of 0.47 eV. Li vacancy (V_{Li}^{-1}) that forms at one of the two unique Li Wyckoff sites is the next dominant defect, with $\Delta E_{D,q}$ of 0.48 eV. These two defects mediating Li diffusion have a total concentration larger than 10^{14} cm^{-3}, indicating a lower Li-ion conductivity than that under Li-rich conditions. The free carrier (electron) concentration is of the order of 10^4 cm^{-3}, which is substantially lower than that under Li-rich conditions.

The formation energy $\Delta E_{D,q}$ changes linearly as the elemental chemical potentials are varied. The moderate Li condition [Fig. 4(b)] represents a scenario where $\Delta\mu_{Li}$ is between the most Li-rich (0.0 eV) and most Li-poor (-0.78 eV) conditions. Compared to the Li-rich condition, $E_{Fermi,eq}$ is now inside the band gap and located at 1.71 eV. The total concentration of the two dominant defects, Li_i^{+1} and V_{Li}^{-1}, are nearly identical to those under the Li-poor conditions. The net free electron concentration is about 10^{10} cm^{-3}. As expected, this concentration is higher than under the Li-poor condition and lower than under the

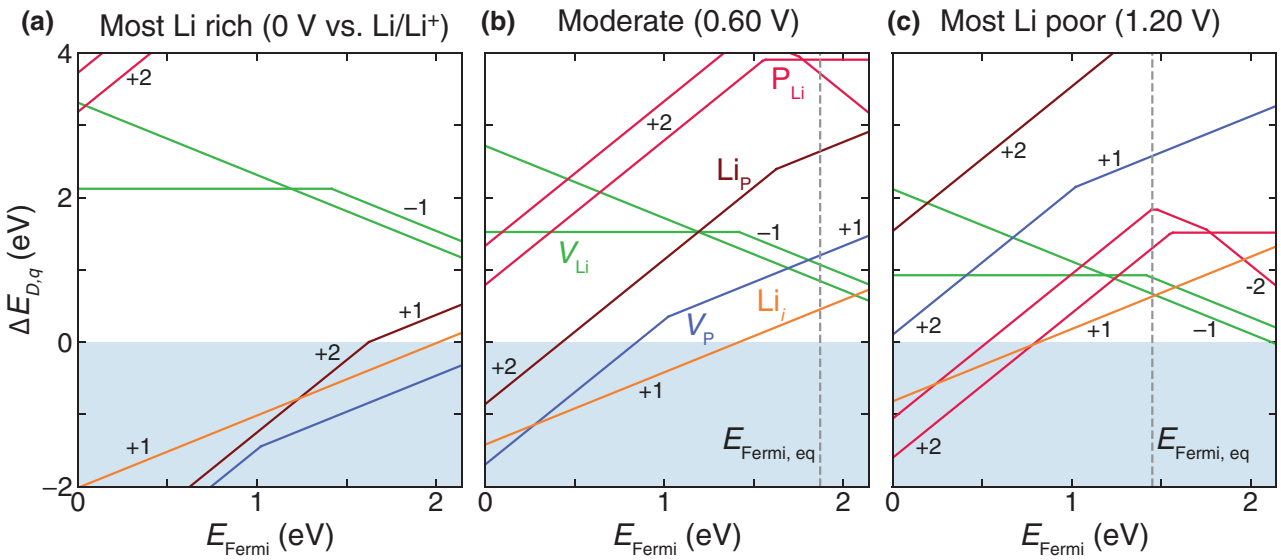

FIG. 5. Formation energy of native point defects in Li_3P as a function of the Fermi energy under (a) the most Li-rich ($\Delta\mu_{Li} = 0$ eV, voltage versus Li/Li^+ is 0.0 V), (b) moderate, and (c) the most Li-poor ($\Delta\mu_{Li} = -1.20$ eV, voltage versus Li/Li^+ is 1.20 V) conditions within the phase stability region constrained by Li and LiP. Multiple lines of the same color represent defects at multiple unique Wyckoff sites.

Li-rich condition. Overall, the net free charge carrier concentration in Li_3N is large, which contributes to the high electronic conductivity of this SEI component.

D. Native defect chemistry of Li_3P

As a potential Li-ion solid conductor, the defect thermodynamics of Li_3P has been the subject of previous studies [33–36]. The high defect concentration in Li_3P was found to provide ionic conductivity higher than 10^{-4} S/cm [33,34]. Our *GW* calculated band gap of Li_3P is 2.14 eV, which is similar to the band gap of Li_3N. The calculated defect energetics of Li_3P are shown in Fig. 5. Like Li_3N, we examine the defect chemistry of Li_3P under the most Li-rich ($\Delta\mu_{Li} = 0$ eV), moderate ($\Delta\mu_{Li} = -0.60$ eV), and most Li-poor ($\Delta\mu_{Li} = -1.20$ eV) thermodynamic conditions.

As in Li_3N, $E_{Fermi,eq}$ for Li_3P under the Li-rich condition [Fig. 5(a)] is inside the conduction band (2.55 eV), and yields a degenerate free electron concentration of 10^{20} cm^{-3}. The dominant defects are V_P^{+1}, Li_i^{+1}, and V_{Li}^{-1}, and the total concentration of defects that mediate Li-ion migration is of the order of 10^{12} cm^{-3}. The energy $E_{Fermi,\,eq}$ moves lower to 1.87 eV under the moderate condition [Fig. 5(b)]. Under the moderate condition, the dominant defects are Li_i^{+1} and V_{Li}^{-1}. Li-ion migration is mainly mediated by these defects with a total concentration of 10^{14} cm^{-3}. Compared to the Li-rich condition, we also find a substantially lower net free electron concentration of 10^{14} cm^{-3}.

Under the most Li-poor or oxidizing conditions [Fig. 5(c)], $E_{Fermi,eq}$ further decreases to 1.45 eV. The dominant defects are the same as those under the moderate conditions, i.e., Li_i^{+1} and V_{Li}^{-1}, and show slightly different $\Delta E_{D,q}$ all below 1 eV. Note that the neutral defect V_{Li}^{0}, not plotted at $E_{Fermi,\,eq}$ because it is less favorable than its charged analogue (V_{Li}^{-1} on the same Wyckoff site), also shows very low $\Delta E_{D,q}$ below 1 eV. All the dominant defects mediating Li diffusion make up a total concentration of 10^{11} cm^{-3}. The net free electron concentration is of the order of 10^{7} cm^{-3}. Li_3P contains substantially fewer Li-related defects that mediate Li-ion diffusion but more net free electrons than Li_3N. Defect and free carrier concentrations in the SEI components are compared in Fig. S2 within the Supplemental Material [27].

E. Native defect chemistry of Li_3PO_4

As the only ternary SEI component, Li_3PO_4 exhibits a more complex phase diagram compared to the binary components. In constructing the phase diagram, we consider all competing phases in the ternary Li-P-O chemical space, including Inorganic Crystal Structure Database (ICSD) phases that are calculated and reported in the NREL Materials Database and the Materials Project [37,38]. The competing phases comprise Li_3P, LiP, Li_3P_7, LiP_7, P, $Li_4P_2O_7$, Li_2O, Li_2O_2, and O_2. By excluding the chemical conditions that favor the formation of these competing phases, we obtain the accessible range of elemental chemical potentials for the stability of Li_3PO_4. In the computed phase diagram (Fig. 6), we find that Li_3PO_4 is not in thermodynamic equilibrium with Li metal ($\Delta\mu_{Li} = 0$ eV).

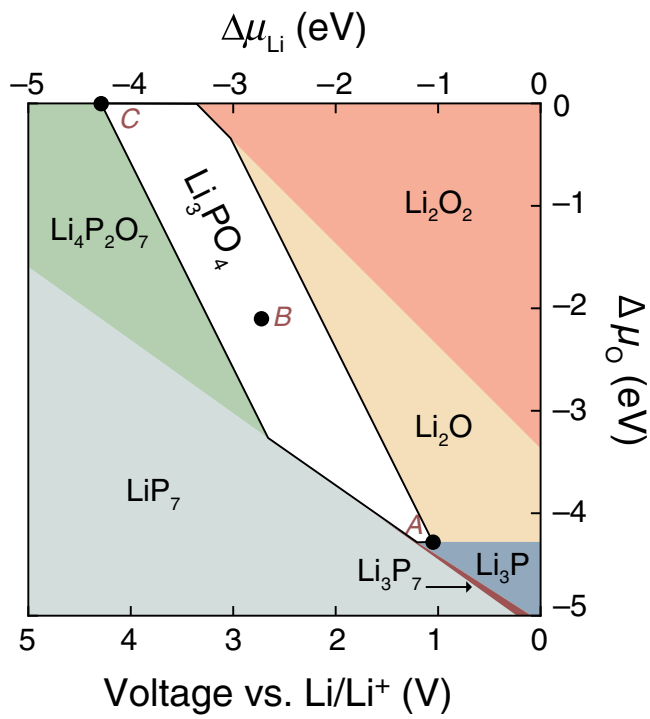

FIG. 6. Phase diagram of Li_3PO_4 based on chemical potential changes of Li ($\Delta\mu_{Li}$) and O ($\Delta\mu_O$). The white region represents the range of chemical potentials where Li_3PO_4 is thermodynamically stable. The most Li-rich, moderate, and the most Li-poor conditions are represented by points A ($\Delta\mu_{Li} = -1.05$ eV, $\Delta\mu_O = -4.28$ eV, $\Delta\mu_P = -0.88$ eV), B ($\Delta\mu_{Li} = -2.67$ eV, $\Delta\mu_O = -2.14$ eV, $\Delta\mu_P = -4.58$ eV), and C ($\Delta\mu_{Li} = -4.29$ eV, $\Delta\mu_O = 0$ eV, $\Delta\mu_P = -8.28$ eV), respectively.

Figure 6 shows the two-dimensional projected phase diagram with $\Delta\mu_{Li}$ and $\Delta\mu_O$ as the axes. For equilibrium growth of Li_3PO_4, $\Delta\mu_P$ depends on the two independent variables by the relationship $3\Delta\mu_{Li} + \Delta\mu_P + 4\Delta\mu_O = \Delta H_f\,(Li_3PO_4)$, where $\Delta H_f\,(Li_3PO_4)$ is the formation enthalpy of Li_3PO_4 (a constant). A voltage axis versus Li/Li^+ is also shown in Fig. 6. Note that we only plot the phases limiting the stability of Li_3PO_4, and phases such as P that do not share boundaries with Li_3PO_4 are not shown. Within the region of phase stability of Li_3PO_4, we have marked three representative points for the most Li-rich (point A, $\Delta\mu_{Li} = -1.05$ eV), moderate (point B, $\Delta\mu_{Li} = -2.67$ eV), and the most Li-poor (point C, $\Delta\mu_{Li} = -4.29$ eV) thermodynamic conditions, respectively.

We calculate the native defect thermodynamics at the limiting points A and C (Fig. 6). The range of the Fermi energy is set by the band gap, which is estimated to be 9.55 eV using the GW approximation. Compared to binary components, the defect plots of Li_3PO_4 (β phase, calculated from ICSD No.10257, space group $Pmn2_1$) are more complex, in part, due to the multiple Wyckoff sites (two Li sites, and three O sites) [39,40], which are indicated by multiple lines of the same color for each defect on Li or O sites in Fig. 7.

Under the Li-rich condition [Fig. 7(a)], $E_{Fermi,eq}$ is at 5.83 eV. The dominant defects are V_O^0, Li_i^{+1}, and V_{Li}^{-1}, but they still show relatively high $\Delta E_{D,q}$ (averaged over all Wyckoff sites) of 0.90, 1.34, and 1.47 eV, respectively. The total concentration of Li_i^{+1} and V_{Li}^{-1}, which mediate Li-ion diffusion, is only 10^{-1} cm^{-3}. These oppositely charged defects are present in almost equal concentrations and lead to charge self-compensation. Therefore, the net free charge carrier concentration is negligible.

Under the most Li-poor or oxidizing condition [Fig. 7(b)], $E_{Fermi,eq}$ is 2.59 eV. The dominant defects are V_{Li}^0, Li_i^{+1}, and V_{Li}^{-1}, with $\Delta E_{D,q}$ all above 1.2 eV. The total concentration of the dominant defects mediating Li-ion diffusion is about 10^2 cm^{-3}. The net free charge carrier concentration is negligible, similar to the Li-rich condition. Even if the "frozen in" temperature for defects is raised to 800 K, the net carrier concentration would only increase to the order of 10^{-25} cm^{-3} (approximately 0.0).

In summary, Li_3PO_4 contains negligible net free charge carriers, with concentrations even lower than Li_2O. The charge carrier concentrations are listed in Table I, and the defect thermodynamics from Secs. II B–II E are summarized in Tables S3–S6 within the Supplemental Material [27].

F. Electronic conductivity of the SEI components

In Secs. II B–II E, we have estimated the charged point defect concentrations for all the Li-LiPON SEI components. Based on these results, we have estimated the room-temperature (300 K) electronic conductivity (σ_e) stemming from the charged point defects under different electrochemical conditions.

According to Eq. (3) below, σ_e is a function of the free charge carrier concentration (n), which is determined from the defect calculations. Because we consider charged defects as the primary source of free charge carriers, n depends on the formation temperature and the prevailing electrochemical conditions. In addition to the charged point defects, polarons may form especially in polarizable materials like Li_2O [41]. If polaronic effects are taken into account for Li_2O, our calculated n will be lowered further because the charge carriers will be trapped as polarons. Consequently, σ_e will be reduced even further. As discussed later, this does not alter our conclusion that Li_2O is an electronic insulator.

The electronic conductivity σ_e is also a function of the carrier mobility (ζ), which is estimated using a semiempirical model [Eq. (4) below] [42]. The error in estimating ζ with the model is $\pm 1/2$ orders of magnitude [42] and has proven to successfully predict σ_e with errors below the experimental variability [25]. The model provides an estimate of the phonon-limited, room temperature ζ_e.

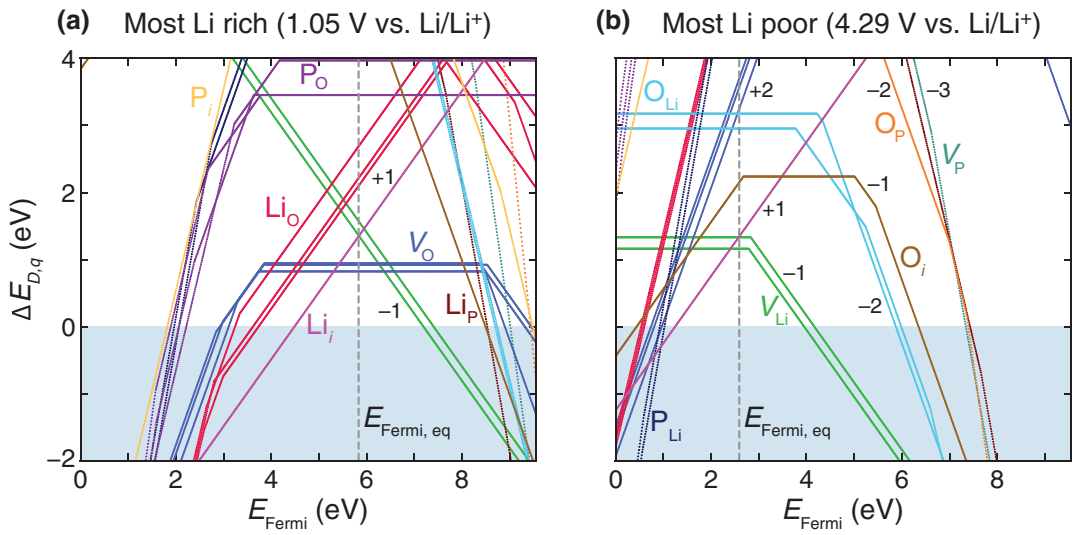

FIG. 7. Formation energy of native point defects in Li_3PO_4 as a function of the Fermi energy under (a) the most Li-rich or reducing ($\Delta\mu_{Li} = -1.05$ eV, voltage versus Li/Li^+ is 1.05 V) and (b) the most Li-poor or oxidizing ($\Delta\mu_{Li} = -4.29$ eV, voltage versus Li/Li^+ is 4.29 V) conditions within the phase stability region constrained by all the competing phases. Multiple lines of the same color represent defects at multiple unique Wyckoff sites.

When combined with n, the room temperature σ_e can be estimated.

Table I lists the electron (ζ_e) and hole mobilities (ζ_h), as well as the electronic conductivity (σ_e) for the four SEI components formed under different electrochemical conditions at $T_{\text{formation}} = 300$ K (data for $T_{\text{formation}} = 500$ K can be found in Table S7 within the Supplemental Material [27]). The electron mobilities are lower in oxides and phosphates compared to those in the nitride and phosphide. Combined with the low predicted free charge carrier concentrations, Li_2O and Li_3PO_4 show negligible electronic conductivity irrespective of the electrochemical conditions. In contrast, Li_3N and Li_3P show very high σ_e reaching 10^1 cm^{-3} and 10^4 cm^{-3}, respectively, at Li-rich conditions. The lower limits of σ_e at the most Li-poor conditions of Li_3N and Li_3P are 10^{-13} cm^{-3} and 10^{-10} cm^{-3}, respectively, which is still non-negligible for a SEI [25]. Large variations in the predicted electronic conductivity arise from different chemical conditions, and predictions are more deterministic when the relevant chemical conditions are known (see Sec. S6 within the Supplemental Material [27]). Note that the free carriers are always electrons in the various materials and electrochemical conditions. Section II B shows a case of Li_2O formed at 800 K (though not achievable in the SEI) where holes become the free carriers. As the chemical condition becomes more

TABLE I. Carrier mobility (ζ) computed with the semiempirical model [Eq. (4) below] for electrons (ζ_e) and holes (ζ_h). The net free charge carrier (electron) concentrations (n) are calculated from defect thermodynamics. Room-temperature electronic conductivity (σ_e) predicted for the SEI components under different thermodynamic conditions. Defects in the SEI components are "frozen in" at the formation temperature ($T_{\text{formation}}$) of 300 K.

SEI	ζ_e (cm^2/Vs)	ζ_h (cm^2/Vs)	Condition	n (cm^{-3})	σ_e (S/cm)
Li_2O	109.0	1.9	Li rich[a]	≈ 0	≈ 0
			Li poor[a]	≈ 0	≈ 0
Li_3N	301.3	4.0	Li rich	2.0×10^{18}	9.9×10^{1}
			moderate[a]	5.8×10^{10}	2.8×10^{-6}
			Li poor	1.6×10^{4}	7.9×10^{-13}
Li_3P	206.2	5.5	Li rich	5.7×10^{20}	1.9×10^{4}
			moderate	2.2×10^{14}	7.2×10^{-3}
			Li poor[a]	2.0×10^{7}	6.5×10^{-10}
Li_3PO_4	92.3	0.7	Li rich[a]	≈ 0	≈ 0
			Li poor[a]	≈ 0	≈ 0

[a]Relevant chemical conditions for each component as observed in experiments [22–24].

Li-rich or the voltage versus Li/Li^+ decreases, σ_e also always increases.

We validate the estimated σ_e by comparing with available experimental data. The electronic conductivity in Li_3N is measured to be 10^{-12} S/cm while Li_3P shows slightly higher σ_e due to the more polarizable P anion [43,44]. The electronic conductivity in Li_2O is reported to have an upper limit of 10^{-14} S/cm; due to measurement limitations, it is possible that σ_e in Li_2O is even lower and therefore negligible. Our estimated σ_e correctly predict the conductive or insulating nature of the SEI components. In summary, Li_3N and Li_3P show worrying electronic conductivities that enable the Li-LiPON interfacial reactions (decomposition of LiPON) and the concomitant SEI formation.

III. DISCUSSION

From first-principles defect calculations, we have obtained the electronic conductivity of the Li-LiPON SEI components Li_2O, Li_3N, Li_3P, and Li_3PO_4 identified from thermodynamic conjectures [9,12,13,22]. Here, we discuss how these results account for the electronic passivation of the interface observed in experiments.

The interfacial reactions between Li and LiPON and the stable nature of the Li-LiPON SEI have been investigated by various microscopy and spectroscopy techniques [22–24]. Schwöbel *et al.* [22] studied the interface layer formation between Li and LiPON using *in situ* XPS. LiPON was exposed to Li vapor, and the reaction products after different exposure time were revealed by the XPS spectra. The authors proposed two reaction routes to describe the reactions between Li and two typical structural units in amorphous LiPON. The proposed reaction routes can be added up to get the chemical equation

$$2Li_6P_3O_9N + 20Li \longrightarrow 2Li_3PO_4 + Li_3P + 10Li_2O + Li_3N. \quad \text{(a)}$$

$Li_6P_3O_9N$ in the reaction formula is only an exemplary chemical structure in the amorphous LiPON, and it does not represent the exact stoichiometry of LiPON, which is presently unknown. Equation (a) gives an approximation of the ratio of the Li-LiPON reaction products. Assuming Eq. (a) has a yield of 100%, the number of moles of Li_2O significantly exceed the other three products, which are expected to only make up a small fraction of the Li-LiPON SEI. In this sense, one can see that the insulating Li_2O (Table I) alone contributes significantly to the nature of the SEI electronic conductivity.

Figure 8 shows the resistance ($R = d/A\sigma_e$) calculated as a function of the SEI thickness d and normalized to an area of $A = 1$ cm^2. For the individual SEI components, the resistance of Li_3N and Li_3P are relatively low

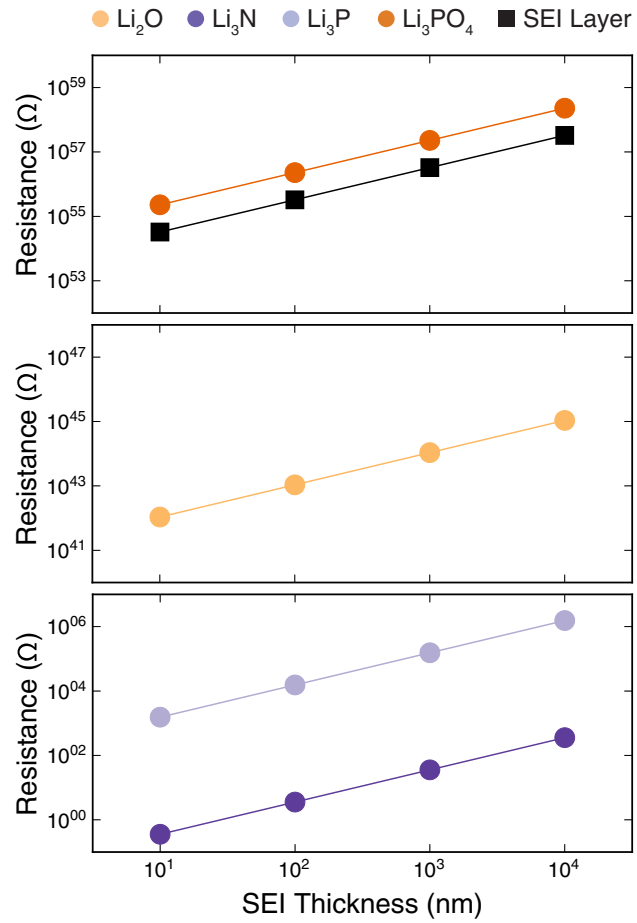

FIG. 8. Resistance as a function of the thickness of the SEI components and the SEI layer at the formation temperature ($T_{\text{formation}}$) of 300 K. The resistance is normalized to an area of 1 cm^2. The SEI layer resistance (black square) is calculated as a weighted average of the SEI component resistance according to the component mass ratio in Eq. (1).

($10^{-1} \sim 10^6$ Ω at 300 K) due to their high electronic conductivity (see Table I). For Li_2O and Li_3PO_4, we used the upper limit of their electronic conductivity (under the Li-rich condition in Table I) to obtain the lower limit of the resistance, which is still significantly high, at least 10^{21} Ω. The SEI layer resistance (black square in Fig. 8) reflects a stoichiometrically weighted average of the resistance of the individual SEI components, according to the mass ratio in Eq. (1). Unsurprisingly, it is close to the highest component resistance (i.e., the Li_3PO_4 resistance), indicating that the SEI layer is insulating. A comparison between the SEI resistance for $T_{\text{formation}}$ of 300 and 500 K can be found in Fig. S2 within the Supplemental Material [27].

Besides the stoichiometric ratio of the decomposition products in Eq. (1), the spatial distribution of the SEI components is also expected to affect the overall SEI electronic conductivity. In a previous study, Schwöbel *et al.* [22] found that the XPS signals indicating the presence of

Li_3N and Li_3P appear on the LiPON surface after short Li vapor exposure, but they then become less intense after longer exposure (> 375 s) and finally disappear. The long-exposure case accounts for LiPON being kept in contact with Li metal. The results indicate that Li_3N and Li_3P could be absent in close proximity to Li metal and only present near the LiPON side of the SEI. While this analysis is undoubtedly powerful, it is limited in shedding light on the electrochemical reactivity of Li-metal with LiPON. Such distribution information excludes the highest σ_e we predicted (10^1–10^4 cm^{-3}) for Li_3N and Li_3P formed under the Li-rich condition. Only the σ_e of Li_3N and Li_3P formed under slightly oxidizing conditions are possible in the SEI. Specifically, we consider the moderate condition ($\Delta\mu_{Li} = -0.39$ eV) for Li_3N as relevant in the SEI, because the Li-poor condition is in equilibrium with N_2, which is difficult to achieve even upon direct contact with LiPON. For Li_3P, we consider the Li-poor condition as relevant in the SEI, as it is in equilibrium with LiP, which is realizable in the SEI. For Li_3N formed under the moderate condition (0.39 V versus Li/Li^+) and Li_3P formed under the Li-poor condition, values of σ_e still appear high (10^{-10}–10^{-3} cm^{-3}) and enable electron diffusion. However, electron conduction can happen only in regions of the SEI where Li_3N and Li_3P nucleate. According to the distribution observed in experiments, Li_3N and Li_3P cannot form near the Li-metal anode. Such evidence suggests that, since Li_3N and Li_3P are buried within the SEI layer and far from the Li-metal anode, electrons cannot "percolate" through the SEI, which inhibits further LiPON decomposition. Therefore, this analysis explains the origin of the apparent "kinetic stabilization" of the Li-LiPON interface.

More recently, Cheng *et al.* [23] have found a similar SEI component distribution using energy dispersive x-ray spectroscopy: Li_2O is distributed throughout the SEI, and Li_3N and Li_3PO_4 are not in direct contact with Li but only distributed in regions closer to LiPON. These results, together with our predicted σ_e, reinforce the idea that the SEI components with high values of σ_e (e.g., Li_3N) are not uniformly distributed in the SEI. Therefore, the SEI is overall electronically insulating, which enables passivation of the Li-LiPON interface.

The study of Hood *et al.* [24] proposed a different component distribution in the SEI structure. A Li-metal tip was put in contact with a LiPON surface and then removed to observe the interfacial evolution. Using *in situ* electron energy-loss spectroscopy (EELS), the authors found that the elements Li and O are distributed throughout the SEI and P is absent near the Li metal contact point, which agrees with the above studies. The difference is that N is dispersed in the SEI, indicating that Li_3N may be present throughout the SEI. However, it is also observed from the EELS elemental maps that the N shows a gridlike or scattered distribution in the SEI layer, in line with the stoichiometric scarcity of Li_3N produced from the LiPON decomposition [Eq. (1)]. Such scarcity and the scattered distribution may not create an electrically continuous path, so the "electrically disconnected" Li_3N particles cannot make the overall SEI electronically conductive.

In the experiments discussed above, the space near Li metal is exclusively occupied by Li_2O. We speculate two plausible reasons. (1) Li_2O formation is thermodynamically more favorable due to its large enthalpy of formation. Experimental observations suggest that Li_2O formation occurs first, which disrupts the amorphous LiPON network, releasing P and N that then react with Li to form Li_3N and Li_3P [22]. (2) It is plausible that the O^{2-} ion is more mobile than N^{3-} and P^{3-} due to its lower charge and smaller ionic radius. Therefore, the migration of O^{2-} may be less impeded than the other anions, leading to faster formation and accumulation of Li_2O close to the Li anode [45,46].

Combining our predicted values of electronic conductivity and the experimental findings discussed above, it is evident that the Li-LiPON SEI is overall electronically insulating, which prevents progressive decomposition of LiPON and stabilizes the Li-LiPON interface. Figure 1 schematically illustrates the hypothesized electronic passivation of the Li-LiPON interface.

In addition to our predicted electronic conductivity, there are other factors contributing to the overall SEI electronic conductivity observed in macroscopic measurements. Previous experiments have suggested that grain boundaries may show higher electronic conductivity than the bulk [47,48]. We are unaware of any universal theory and computational model to estimate the electronic conductivity in grain boundaries. It is an exciting avenue for future developments.

From our defect calculations, we also obtained the total concentrations of the defects that can mediate Li ion diffusion (Tables S3–S6 within the Supplemental Material [27]), which is a good indicator of ionic conductivity. Indeed, for the two SEI components with high Li ionic conductivity, namely Li_3N (10^{-3} S/cm) and Li_3P (10^{-4} S/cm), we predict high Li-related defect concentrations of 10^{14}–10^{15} and 10^{11}–10^{14} cm^{-3}, respectively [29,33]. Li_2O exhibits low ionic conductivity of 10^{-12} S/cm, which is in agreement with our predicted low Li-related defect concentration in the range 10^2–10^5 cm^{-3} [49]. We predict a low defect concentration in β-Li_3PO_4, which is consistent with the measured low ionic conductivity [50,51].

IV. CONCLUSIONS

We demonstrated a computational approach to assessing the electronic passivation of SEIs and stability of solid-solid interfaces in ASSBs. Specifically, we used first-principles calculations to determine the concentrations of point defects and charge carriers in the Li-LiPON SEIs, and demonstrated that the interfacial stability arises

from electronic passivation of the SEI layer. In calculating the defect and charge carrier concentrations, we considered different (electro)chemical conditions in the 300–500 K temperature range. Combining the experimentally observed spatial distribution of the different SEI components, we identified their relevant chemical conditions in the SEI layer. Under the relevant moderate Li chemical potential condition, Li_3N shows high electronic conductivity up to about $10^{-6} \sim 10^{-3}$ S/cm in the temperature range of interest. Li_3P is effectively under the Li-poor condition in the SEI layer, and it shows considerable electronic conductivity of $10^{-10} \sim 10^{-5}$ S/cm. Across the chemical conditions from Li rich (reducing) to Li poor (oxidizing), Li_2O and Li_3PO_4 show negligible carrier concentrations and electronic conductivity arising from the defects. We reveal that the overall SEI layer is electronically insulating because the stoichiometrically abundant and uniformly distributed Li_2O is insulating, while the electronically conducting Li_3N and Li_3P were previously found to be absent near the Li-metal anode or nonuniformly distributed in the SEI. These findings provide evidence for the hypothesis that the Li-LiPON interface is stabilized due to the formation of electronically passivated SEI that prevents further LiPON decomposition. While we have focused on the Li-LiPON interface, our case study demonstrates a computational approach that can effectively complement experimental investigations of interfacial stability in ASSBs. We expect this study to stimulate future investigations on the interfacial stability for other solid electrolytes and interphases.

V. METHODOLOGY

In each SEI component, we investigate native charged point defects, including vacancies (e.g., Li vacancy in charge state -1, V_{Li}^{-1}), interstitials (e.g., Li interstitial in charge state $+1$, Li_i^{+1}), and antisites (e.g., Li on the O site in charge state $+1$, $\mathrm{Li}_{\mathrm{O}}^{+1}$). Vacancies and antisites at each Wyckoff site are treated as distinct defects. For interstitial defects, the plausible sites are determined by a Voronoi tessellation scheme as implemented in the pylada-defects package [52]. At least five interstitial sites are identified for each SEI component. The lowest-energy interstitial site is determined from the total energy of the interstitial configurations in the neutral charge state. A broad set of charge states are considered for each defect type, typically $q = -3, -2, -1, 0, +1, +2$, and $+3$. Additional charge states are considered where necessary. The defect formation energy $\Delta E_{D,q}$ of a point defect D in charge state q is calculated as

$$\Delta E_{D,q} = E_{D,q} - E_{\mathrm{bulk}} - \sum_i n_i \mu_i + q E_{\mathrm{Fermi}} + E_{\mathrm{corr}}, \quad (1)$$

where $E_{D,q}$ and E_{bulk} are the total energies of defected and pristine supercells, respectively; μ_i is the chemical potential of element i, and n_i is the number of atoms of element i added ($n_i > 0$) or removed ($n_i < 0$) from the pristine supercell to create defect D; E_{Fermi} is the Fermi energy, which is referenced to the valence-band maximum; E_{corr} is the correction to the defect formation energy to account for the finite-size effects and underestimation of the band gap. Following the methodology of Lany and Zunger [53], we include the following finite-size corrections: (i) alignment of the average electrostatic potential between supercells with and without charged defects, (ii) long-range electrostatic interactions between periodic images of point charges, and (iii) band filling due to shallow defects.

Total energies are calculated with density functional theory (DFT) approximated by the Perdew-Burke-Ernzerhof functional [54,55]. The wavefunctions are expanded as plane waves, and the projector-augmented-wave potentials are used for describing core electrons [56–59]: Li_sv 23Jan2001, P 17Jan2003, O_s 07Sep2000, and N_s 07Sep2000. A plane-wave cutoff energy of 340 eV is used for all the calculations. Initial structures are taken from the ICSD: Li_2O (ICSD No.057411), Li_3N (ICSD No.34675), Li_3P (ICSD No.240861), and Li_3PO_4 (ICSD No.10257). First, the primitive cells are fully relaxed with Γ-centered k-point grids automatically generated with a length parameter of 10. Next, supercells are constructed from the relaxed primitive cells. Supercells containing 96 atoms (Li_2O), 108 atoms (Li_3N), 144 atoms (Li_3P), and 128 atoms (Li_3PO_4) are used. The atomic positions in the defect supercells are relaxed while keeping the volume and cell shape fixed. Defect supercell relaxations are performed with a Γ-centered $2 \times 2 \times 2$ Monkhorst pack k-point grid for Li_3P and a $4 \times 4 \times 4$ grid for the others with fewer atoms in the supercells.

To address the underestimation of band gaps by DFT, individual valence- and conduction-band edge shifts (relative to the DFT-computed band edges) are determined from GW quasiparticle energy calculations using a methodology detailed in Ref. [25]. We use dense k-point grids to sample the band edges in GW calculations. Specifically, we use a Γ-centered $12 \times 12 \times 12$ k-point grid for Li_2O, $12 \times 12 \times 10$ for Li_3N, $10 \times 10 \times 10$ for Li_3P, and $6 \times 6 \times 8$ for Li_3PO_4. The calculations are set up, managed, and analyzed with the pylada-defects software package [52].

The electronic conductivity (σ_e) is estimated in the framework of Drude theory [60] of Eq. (2)

$$\sigma_e = ne\zeta. \quad (2)$$

Here n is the concentration of free charge carriers (electrons or holes) arising from the formation of charged point defects, e is the electronic charge, and ζ is the carrier mobility. We estimate ζ using a semiempirical

model with parameters that are fitted to experimentally measured room-temperature carrier mobilities [42]. The model inputs, including bulk modulus and band effective mass, can be obtained from DFT calculations. The carrier mobility ζ is estimated as

$$\zeta = A_0 B^s (m_b^*)^{-t}, \tag{3}$$

where A_0, s, and t are fitted constants; B is the bulk modulus obtained from the Birch-Murnaghan equation fitted to DFT calculated volumes and energies for unit cells around the equilibrium volume; m_b^* is the band effective mass calculated as $m_b^* = N_b^{2/3} m_{\mathrm{DOS}}^*$, where m_{DOS}^* is the density-of-state (DOS) effective mass, extracted within a 100-meV energy window from the band edge, and N_b is the band degeneracy. The band here refers to the conduction band for electrons and the valence band for holes. Parabolic bands and isotropic transport are assumed. Note that the estimated ζ represents the intrinsic phonon-limited upper limit of the carrier mobility, and consequently the estimated σ_e is also treated as the upper limit of electronic conductivity.

ACKNOWLEDGMENTS

P.C. acknowledges funding from National Research Foundation Program NRFF12-2020-0012. P.G. acknowledges funding from the Laboratory Directed Research and Development (LDRD) program at NREL. The computational work was performed on resources of the National Supercomputing Centre, Singapore. The research was also supported in part through computational resources sponsored by the U.S. Department of Energy's Office of Energy Efficiency and Renewable Energy and located at NREL.

[1] B. Dunn, H. Kamath, and J.-M. Tarascon, Electrical energy storage for the grid: A battery of choices, Science **334**, 928 (2011).

[2] B. Nykvist and M. Nilsson, Rapidly falling costs of battery packs for electric vehicles, Nat. Clim. Chang. **5**, 329 (2015).

[3] Z. P. Cano, D. Banham, S. Ye, A. Hintennach, J. Lu, M. Fowler, and Z. Chen, Batteries and fuel cells for emerging electric vehicle markets, Nat. Energy **3**, 279 (2018).

[4] J. B. Goodenough and Y. Kim, Challenges for rechargeable Li batteries, Chem. Mater. **22**, 587 (2010).

[5] J. C. Bachman, S. Muy, A. Grimaud, H.-H. Chang, N. Pour, S. F. Lux, O. Paschos, F. Maglia, S. Lupart, P. Lamp, L. Giordano, and Y. Shao-Horn, Inorganic solid-state electrolytes for lithium batteries: Mechanisms and properties governing ion conduction, Chem. Rev. **116**, 140 (2016).

[6] Z. Zhang, Y. Shao, B. Lotsch, Y.-S. Hu, H. Li, J. Janek, L. F. Nazar, C.-W. Nan, J. Maier, M. Armand, and L. Chen, New horizons for inorganic solid state ion conductors, Energy Environ. Sci. **11**, 1945 (2018).

[7] J. Janek and W. G. Zeier, A solid future for battery development, Nat. Energy **1**, 16141 (2016).

[8] T. Famprikis, P. Canepa, J. A. Dawson, M. S. Islam, and C. Masquelier, Fundamentals of inorganic solid-state electrolytes for batteries, Nat. Mater. **18**, 1278 (2019).

[9] W. D. Richards, L. J. Miara, Y. Wang, J. C. Kim, and G. Ceder, Interface stability in solid-state batteries, Chem. Mater. **28**, 266 (2016).

[10] L. Porz, T. Swamy, B. W. Sheldon, D. Rettenwander, T. Frömling, H. L. Thaman, S. Berendts, R. Uecker, W. C. Carter, and Y.-M. Chiang, Mechanism of lithium metal penetration through inorganic solid electrolytes, Adv. Energy. Mater. **7**, 1701003 (2017).

[11] Y. Xiao, Y. Wang, S.-H. Bo, J. C. Kim, L. J. Miara, and G. Ceder, Understanding interface stability in solid-state batteries, Nat. Rev. Mater. **5**, 105 (2020).

[12] Y. Zhu, X. He, and Y. Mo, Origin of outstanding stability in the lithium solid electrolyte materials: Insights from thermodynamic analyses based on first-principles calculations, ACS Appl. Mater. Interfaces **7**, 23685 (2015).

[13] Y. Zhu, X. He, and Y. Mo, First principles study on electrochemical and chemical stability of solid electrolyte–electrode interfaces in all-solid-state Li-ion batteries, J. Mater. Chem. A **4**, 3253 (2016).

[14] J. Bates, Electrical properties of amorphous lithium electrolyte thin films, Solid State Ionics **53–56**, 647 (1992).

[15] J. Bates, N. Dudney, G. Gruzalski, R. Zuhr, A. Choudhury, C. Luck, and J. Robertson, Fabrication and characterization of amorphous lithium electrolyte thin films and rechargeable thin-film batteries, J. Power Sources **43**, 103 (1993).

[16] J. Bates, G. Gruzalski, N. Dudney, C. Luck, and X. Yu, Rechargeable thin-film lithium batteries, Solid State Ionics **70–71**, 619 (1994).

[17] J. Bates, N. Dudney, D. Lubben, G. Gruzalski, B. Kwak, X. Yu, and R. Zuhr, Thin-film rechargeable lithium batteries, J. Power Sources **54**, 58 (1995).

[18] X. Yu, J. B. Bates, G. E. Jellison, and F. X. Hart, A stable thin-film lithium electrolyte: Lithium phosphorus oxynitride, J. Electrochem. Soc. **144**, 524 (1997).

[19] J. Bates, Thin-film lithium and lithium-ion batteries, Solid State Ionics **135**, 33 (2000).

[20] V. Lacivita, A. S. Westover, A. Kercher, N. D. Phillip, G. Yang, G. Veith, G. Ceder, and N. J. Dudney, Resolving the amorphous structure of lithium phosphorus oxynitride (Lipon), J. Am. Chem. Soc. **140**, 11029 (2018).

[21] J. Li, C. Ma, M. Chi, C. Liang, and N. J. Dudney, Solid electrolyte: The key for high-voltage lithium batteries, Adv. Energy Mater. **5**, 1401408 (2015).

[22] A. Schwöbel, R. Hausbrand, and W. Jaegermann, Interface reactions between LiPON and lithium studied by in-situ *X*-ray photoemission, Solid State Ionics **273**, 51 (2015).

[23] D. Cheng, T. A. Wynn, X. Wang, S. Wang, M. Zhang, R. Shimizu, S. Bai, H. Nguyen, C. Fang, M.-c. Kim, W. Li, B. Lu, S. J. Kim, and Y. S. Meng, Unveiling the stable nature of the solid electrolyte interphase between lithium metal and LiPON via cryogenic electron microscopy, Joule **4**, 2484 (2020).

[24] Z. D. Hood, X. Chen, R. L. Sacci, X. Liu, G. M. Veith, Y. Mo, J. Niu, N. J. Dudney, and M. Chi, Elucidating interfacial stability between lithium metal anode and Li phosphorus oxynitride via *in situ* electron microscopy, Nano Lett. **21**, 151 (2021).

[25] P. Gorai, T. Famprikis, B. Singh, V. Stevanović, and P. Canepa, Devil is in the defects: Electronic conductivity in solid electrolytes, Chem. Mater. **33**, 7484 (2021).

[26] S. P. Ong, L. Wang, B. Kang, and G. Ceder, Li-Fe-P-O_2 phase diagram from first principles calculations, Chem. Mater. **20**, 1798 (2008).

[27] See Supplemental Material at http://link.aps.org/supplemental/10.1103/PRXEnergy.1.023004 for the accuracy of calculated formation enthalpy and the effect on defect thermodynamics, which includes Refs. [37,61]; for complete lists of defect and charge carrier concentrations; for the density of states of pristine and defective Li_2O; for plots of defect and carrier concentrations in Li_3N and Li_3P; for electronic conductivity at $T_{\text{formation}}$ of 500 K, which includes Refs. [22–24]; for variations in predicted electronic conductivity, which includes Refs. [62–64]; and for SEI resistance at $T_{\text{formation}}$ of 300 and 500 K.

[28] P. Canepa, G. Sai Gautam, D. Broberg, S.-H. Bo, and G. Ceder, Role of point defects in spinel Mg chalcogenide conductors, Chem. Mater. **29**, 9657 (2017).

[29] U. v. Alpen, A. Rabenau, and G. H. Talat, Ionic conductivity in Li_3N single crystals, Appl. Phys. Lett. **30**, 621 (1977).

[30] U. Alpen, Li_3N: A promising Li ionic conductor, J. Solid State Chem. **29**, 379 (1979).

[31] T. Lapp, Ionic conductivity of pure and doped Li_3N, Solid State Ionics **11**, 97 (1983).

[32] W. Li, G. Wu, C. M. Araújo, R. H. Scheicher, A. Blomqvist, R. Ahuja, Z. Xiong, Y. Feng, and P. Chen, Li^+ ion conductivity and diffusion mechanism in α-Li_3 N and β-Li_3N, Energy Environ. Sci. **3**, 1524 (2010).

[33] G. Nazri, Preparation, structure and ionic conductivity of lithium phosphide, Solid State Ionics **34**, 97 (1989).

[34] G. Nazri, R. Conell, and C. Julien, Preparation and physical properties of lithium phosphide-lithium chloride, a solid electrolyte for solid state lithium batteries, Solid State Ionics **86–88**, 99 (1996).

[35] L. Lin, F. Liang, K. Zhang, H. Mao, J. Yang, and Y. Qian, Lithium phosphide/lithium chloride coating on lithium for advanced lithium metal anode, J. Mater. Chem. A **6**, 15859 (2018).

[36] N. Wu, Y. Li, A. Dolocan, W. Li, H. Xu, B. Xu, N. S. Grundish, Z. Cui, H. Jin, and J. B. Goodenough, In situ formation of Li_3 P layer enables fast Li^+ conduction across Li/solid polymer electrolyte interface, Adv. Funct. Mater. **30**, 2000831 (2020).

[37] V. Stevanović, S. Lany, X. Zhang, and A. Zunger, Correcting density functional theory for accurate predictions of compound enthalpies of formation: Fitted elemental-phase reference energies, Phys. Rev. B **85**, 115104 (2012).

[38] A. Jain, S. P. Ong, G. Hautier, W. Chen, W. D. Richards, S. Dacek, S. Cholia, D. Gunter, D. Skinner, G. Ceder, and K. A. Persson, Commentary: The Materials Project: A materials genome approach to accelerating materials innovation, APL Mater. **1**, 011002 (2013).

[39] N. D. Lepley, N. A. W. Holzwarth, and Y. A. Du, Structures, Li^+ mobilities, and interfacial properties of solid electrolytes Li_3PS_4 and Li_3PO_4 from first principles, Phys. Rev. B **88**, 104103 (2013).

[40] N. Ishigaki and J. Akimoto, Room temperature synthesis and phase transformation of lithium phosphate Li_3PO_4 as solid electrolyte, J. Asian Ceram. Soc. **9**, 452 (2021).

[41] C. Franchini, M. Reticcioli, M. Setvin, and U. Diebold, Polarons in materials, Nat. Rev. Mater. **6**, 560 (2021).

[42] J. Yan, P. Gorai, B. Ortiz, S. Miller, S. A. Barnett, T. Mason, V. Stevanović, and E. S. Toberer, Material descriptors for predicting thermoelectric performance, Energy Environ. Sci. **8**, 983 (2015).

[43] J. Wahl, Ionic conductivity of lithium nitride doped with hydrogen, Solid State Commun. **29**, 485 (1979).

[44] G. Nazri, Preparation, characterization and conductivity of Li_3 N, Li_3 P and Li_3 As, MRS Proc. **135**, 117 (1988).

[45] Z. Rong, R. Malik, P. Canepa, G. Sai Gautam, M. Liu, A. Jain, K. Persson, and G. Ceder, Materials design rules for multivalent ion mobility in intercalation structures, Chem. Mater. **27**, 6016 (2015).

[46] Z. Deng, G. Sai Gautam, S. K. Kolli, J.-N. Chotard, A. K. Cheetham, C. Masquelier, and P. Canepa, Phase behavior in rhombohedral NaSiCON electrolytes and electrodes, Chem. Mater. **32**, 7908 (2020).

[47] F. Han, A. S. Westover, J. Yue, X. Fan, F. Wang, M. Chi, D. N. Leonard, N. J. Dudney, H. Wang, and C. Wang, High electronic conductivity as the origin of lithium dendrite formation within solid electrolytes, Nat. Energy **4**, 187 (2019).

[48] Y. Song, L. Yang, W. Zhao, Z. Wang, Y. Zhao, Z. Wang, Q. Zhao, H. Liu, and F. Pan, Revealing the short-circuiting mechanism of garnet-based solid-state electrolyte, Adv. Energy Mater. **9**, 1900671 (2019).

[49] S. Lorger, R. Usiskin, and J. Maier, Transport and charge carrier chemistry in lithium oxide, J. Electrochem. Soc. **166**, A2215 (2019).

[50] Y. A. Du and N. A. W. Holzwarth, Mechanisms of Li^+ diffusion in crystalline γ- and β-Li_3PO_4 electrolytes from first principles, Phys. Rev. B **76**, 174302 (2007).

[51] Y. Deng, C. Eames, J.-N. Chotard, F. Lalère, V. Seznec, S. Emge, O. Pecher, C. P. Grey, C. Masquelier, and M. S. Islam, Structural and mechanistic insights into fast lithium-ion conduction in Li_4SiO_4–Li_3PO_4 solid electrolytes, J. Am. Chem. Soc. **137**, 9136 (2015).

[52] A. Goyal, P. Gorai, H. Peng, S. Lany, and V. Stevanović, A computational framework for automation of point defect calculations, Comput. Mater. Sci. **130**, 1 (2017).

[53] S. Lany and A. Zunger, Assessment of correction methods for the band-gap problem and for finite-size effects in supercell defect calculations: Case studies for ZnO and GaAs, Phys. Rev. B **78**, 235104 (2008).

[54] W. Kohn and L. J. Sham, Self-consistent equations including exchange and correlation effects, Phys. Rev. **140**, A1133 (1965).

[55] J. P. Perdew, K. Burke, and M. Ernzerhof, Generalized Gradient Approximation Made Simple, Phys. Rev. Lett. **77**, 3865 (1996).

[56] G. Kresse and J. Furthmüller, Efficiency of ab-initio total energy calculations for metals and semiconductors using a plane-wave basis set, Comput. Mater. Sci. **6**, 15 (1996).

[57] G. Kresse and J. Furthmüller, Efficient iterative schemes for *ab initio* total-energy calculations using a plane-wave basis set, Phys. Rev. B **54**, 11169 (1996).

[58] P. E. Blöchl, Projector augmented-wave method, Phys. Rev. B **50**, 17953 (1994).

[59] G. Kresse and D. Joubert, From ultrasoft pseudopotentials to the projector augmented-wave method, Phys. Rev. B **59**, 1758 (1999).

[60] C. Kittel and D. F. Holcomb, Introduction to solid state physics, Am. J. Phys. **35**, 547 (1967).

[61] D. D. Wagman, W. H. Evans, V. B. Parker, R. H. Schumm, I. Halow, S. M. Bailey, K. L. Churney, and R. L. Nuttall, The NBS tables of chemical thermodynamic properties, J. Phys. Chem. Ref. Data **11**, Supplement No. 2 (1982).

[62] S. Zhang, S.-H. Wei, and A. Zunger, A phenomenological model for systematization and prediction of doping limits in II–VI and I–III–VI2 compounds, J. Appl. Phys. **83**, 3192 (1998).

[63] D. Holmes, R. Chen, K. Elliott, and C. Kirkpatrick, Stoichiometry-controlled compensation in liquid encapsulated Czochralski GaAs, Appl. Phys. Lett. **40**, 46 (1982).

[64] G. Jeong, J. Kim, O. Gunawan, S. R. Pae, S. H. Kim, J. Y. Song, Y. S. Lee, and B. Shin, Preparation of single-phase snse thin-films and modification of electrical properties via stoichiometry control for photovoltaic application, J. Alloys Compd. **722**, 474 (2017).